

## Reinforced polysulfide barrier by g-C<sub>3</sub>N<sub>4</sub>/CNT composite towards superior lithium-sulfur batteries

Xiangliang Wang<sup>a,1</sup>, Gaoran Li<sup>b,1</sup>, Minjie Li<sup>a</sup>, Ruiping Liu<sup>a,\*</sup>, Haibo Li<sup>c</sup>, Tengyu Li<sup>a</sup>, Mingzhu Sun<sup>c</sup>, Yirui Deng<sup>a</sup>, Ming Feng<sup>c,\*</sup>, Zhongwei Chen<sup>b,\*</sup>

<sup>a</sup> Department of Materials Science and Engineering, China University of Mining & Technology (Beijing), Beijing 100083, China

<sup>b</sup> Department of Chemical Engineering, University of Waterloo, Waterloo N2L 3G1, ON, Canada

<sup>c</sup> Key Laboratory of Functional Materials Physics and Chemistry of the Ministry of Education, Jilin Normal University, Changchun, 130103 Jilin, China

### ARTICLE INFO

#### Article history:

Received 30 April 2020

Revised 18 May 2020

Accepted 18 May 2020

Available online 23 May 2020

#### Keywords:

Graphitic carbon nitride  
Reinforced separator  
Lithium sulfur battery  
Chemical interaction  
Synergistic effect

### ABSTRACT

The notorious shuttle effect has long been obstructing lithium-sulfur (Li-S) batteries from yielding the expected high energy density and long lifespan. Herein, we develop a multifunctional polysulfide barrier reinforced by the graphitic carbon nitride/carbon nanotube (g-C<sub>3</sub>N<sub>4</sub>/CNT) composite toward inhibited shuttling behavior and improved battery performance. The obtained g-C<sub>3</sub>N<sub>4</sub> delivers a unique sponge-like architecture with massive ion transfer pathways and fully exposed active interfaces, while the abundant C-N heteroatomic structures impose strong chemical immobilization toward lithium polysulfides. Combined with the highly conductive agent, the g-C<sub>3</sub>N<sub>4</sub>/CNT reinforced separator is endowed with great capability of confining and reutilizing the active sulfur within the cathode, thus contributing to an efficient and stable sulfur electrochemistry. Benefiting from these synergistic attributes, Li-S cells based on g-C<sub>3</sub>N<sub>4</sub>/CNT separator exhibit an excellent cyclability with a minimum decay rate of 0.03% per cycle over 500 cycles and decent rate capability up to 2 C. Moreover, a high areal capacity of 7.69 mAh cm<sup>-2</sup> can be achieved under a raised sulfur loading up to 10.1 mg cm<sup>-2</sup>, demonstrating a facile and efficient pathway toward superior Li-S batteries.

© 2020 Science Press and Dalian Institute of Chemical Physics, Chinese Academy of Sciences. Published by ELSEVIER B.V. and Science Press. All rights reserved.

## 1. Introduction

The ever-increasing energy demand has been appealing for serious advances in energy storage technologies. In such a context, lithium-sulfur (Li-S) batteries have aroused great research interests worldwide as a highly promising next-generation battery system, owing to their high energy density (2600 Wh kg<sup>-1</sup>), as well as the natural abundance, low cost, and environmental benignity of sulfur [1–5]. Despite the convincing advantages, the practical implementation of this technology is still perplexed by several technical challenges, involving the poor electrical/ionic conductivity of sulfur and its lithiation products, large volume variation upon the battery operation, and more particularly, the shuttle effect induced by the dissolution and migration of the intermediate lithium polysulfides (LiPS), which result in poor reaction efficiency and limited battery lifespan [6–10].

In the past few decades, multifarious strategies have been exploited to address these issues. Among them, one major solution lies in the development of conductive and nanostructured sulfur host materials, such as various carbons [11,12], transition-metal oxides/nitrides/sulfides [13–15], Mxene [16] and MOFs [17]. The introduction of these host materials not only enhances the overall conductivity that facilitates the sulfur electrochemical reactions, but also restrains the dissolution and diffusion behaviors of LiPS via the physical and/or chemical interactions toward inhibited shuttle effect. Recently, the separator modification on the cathodic side has been emerging as another promising approach for further enhancement of Li-S battery performance. Rational separator modifiers are required to establish a multifunctional barrier against the migration of LiPS into the anode, thus suppressing the overall shuttle effect. Carbon-based materials such as carbon nanotubes (CNT) [18], graphene [19], porous carbon [20], etc., currently dominate the separator modifications due to their excellent conductivity, high porosity, and good processability. The carbon-modified separators not only physically obstruct the LiPS penetration, but also serve as a secondary current collector for decreased internal resistance and enhanced sulfur reutilization, thus rendering promoted

\* Corresponding authors.

E-mail addresses: [lrp@cumtb.edu.cn](mailto:lrp@cumtb.edu.cn) (R. Liu), [mingfeng@jlnu.edu.cn](mailto:mingfeng@jlnu.edu.cn) (M. Feng), [zhwchen@uwaterloo.ca](mailto:zhwchen@uwaterloo.ca) (Z. Chen).

<sup>1</sup> These authors contributed equally to this work.

and stabilized sulfur reactions. Nevertheless, the nonpolar nature of carbon materials fails to implement a sufficiently strong sulfur immobilization ascribed to their limited affinity to the weak-polar LiPS, which stimulates the active explorations of polar materials in separator designs for further polysulfide regulation.

Inspired by the success of heteroatom-doped carbons in chemical sulfur confinement, graphitic carbon nitride ( $\text{g-C}_3\text{N}_4$ ) presents a highly promising separator modifier in Li-S batteries. While holding a planer lattice structure similar to graphitic carbon,  $\text{g-C}_3\text{N}_4$  contrastively delivers a high content of C-N heteroatom moieties. The massive implantation of highly electron-drawing N breaks the even charge distribution in carbon planes and induces a considerable polar surface for  $\text{g-C}_3\text{N}_4$ , which is expected with enhanced LiPS affinity compared with carbon materials via stronger dipolar-dipolar interactions [21]. Apart from that,  $\text{g-C}_3\text{N}_4$  also holds advantages of light weight and high porosity over the popularly-studied inorganic LiPS adsorbents such as metal oxides, carbides, sulfides, and nitrides. In view of these benefits, several attempts of cathode construction or separator modification by  $\text{g-C}_3\text{N}_4$  have been explored with considerable improvements [22–27]. However, the generally planar or particulate  $\text{g-C}_3\text{N}_4$  suffers from either insufficient physical sulfur accommodation or limited active site exposure. In addition, the intrinsic demerit of the unsatisfactory conductivity of  $\text{g-C}_3\text{N}_4$  is another major issue that impedes its successful implementation in Li-S batteries.

In this contribution, a composite reinforcement by the  $\text{g-C}_3\text{N}_4$  micro-sponge and carbon nanotube (CNT) was developed via a facile filtration method to construct a multifunctional separator for the shuttle inhibition and electrochemical improvement in Li-S batteries. The curled, coherent and porous  $\text{g-C}_3\text{N}_4$  in sponge-like microstructure not only favors the facile ion/mass transfer, but also renders strong sulfur immobilizations through its physical and chemical interactions with LiPS. Meanwhile, the incorporation of CNT establishes an interconnected conductive framework, which well overcomes the non-conductive demerit of  $\text{g-C}_3\text{N}_4$  and facilitates a fast sulfur redox reactions. Consequently, the as-developed reinforced separator effectively inhibits the shuttling behaviors and enhances the sulfur utilization, contributing to a significantly improved Li-S battery performance, i.e., excellent cycling stability over 500 cycles with a slight capacity decay of 0.03% per cycle, decent rate performance up to 2 C, and commendable areal capacity of  $7.69 \text{ mAh cm}^{-2}$  under raised sulfur loading.

## 2. Experimental

### 2.1. Preparation of $\text{g-C}_3\text{N}_4$ and $\text{g-C}_3\text{N}_4/\text{CNT@PP}$ separator

The  $\text{g-C}_3\text{N}_4$  was prepared through a thermal condensation method. Typically, 15 g urea was placed in an aluminum oxide crucible with cover and subject to annealing at  $550^\circ\text{C}$  for 6 h with a ramping rate of  $2^\circ\text{C min}^{-1}$ . Pale-yellow  $\text{g-C}_3\text{N}_4$  was obtained after cooling. To prepare the modified separator,  $\text{g-C}_3\text{N}_4$  and CNT in weight ratio of 1:1 were homogeneously dispersed by sonication in a water-ethanol mixed solvent (1:2 by volume) containing 10 wt% LA133 (to the mass of  $\text{g-C}_3\text{N}_4$ ) as binder for improved mechanical robustness. The precursor solution was then vacuum filtrated onto the PP membrane to obtain the  $\text{g-C}_3\text{N}_4/\text{CNT@PP}$  composite separator. The mass loading was controlled at around  $0.45 \text{ mg cm}^{-2}$ . For comparison,  $\text{g-C}_3\text{N}_4/\text{SP@PP}$  and  $\text{g-C}_3\text{N}_4@\text{PP}$  separators were also prepared respectively by replacing CNT with SP and not using conductive additive.

### 2.2. Preparation of the sulfur/CNT composite electrodes

The S/CNT composite was prepared through the conventional melt-diffusion method. Sublimed sulfur and CNT were uniformly

mixed in weight ratio of 1:3 and subject to annealing at  $155^\circ\text{C}$  for 12 h. The S/CNT electrodes were prepared by casting the homogeneous slurry containing S/CNT, super P, and polyvinylidene fluoride (PVDF) in weight ratio of 8:1:1 onto Al foil. The electrodes were vacuum dried under  $60^\circ\text{C}$  overnight before use. The electrode foil was cut into disks with a diameter of 12 mm for the cell fabrication. The typical sulfur loading on the electrodes was  $1.4 \text{ mg cm}^{-2}$ , while electrodes with higher sulfur loadings were also prepared to pursue higher energy density.

### 2.3. Material characterizations

Field Emission Scanning Electron Microscope (FESEM, Gemini SEM 500) and Transmission Electron Microscope (TEM, JEM-2010) were used to observe the morphologies of  $\text{g-C}_3\text{N}_4$  and the modified separator. The phase compositions were determined by XRD (Bruker D8). The porous texture of  $\text{g-C}_3\text{N}_4$  was analyzed by the  $\text{N}_2$  adsorption-desorption using a NOVA4000 automated system. XPS spectra were collected an ESCALAB 250Xi with an Al  $K_\alpha$  X-ray radiation to study the surface chemistry of the samples. UV-vis spectra were recorded by METASH UV9000s UV-Visible spectrophotometer.

### 2.4. Electrochemical characterizations

The coin cells (CR2032) with different separators were assembled in an Ar-filled glove box (Mikrouna, Shanghai, China) by using S/CNT electrodes as cathode and lithium foil as anode. The electrolyte contains 1 M bis(trifluoromethanesulfonyl)imide lithium (LiTFSI) in a binary solvent of 1, 2-dimethoxyethane (DME) and 1, 3-dioxolane (DOL) (1:1 by volume) with  $\text{LiNO}_3$  additive (1 wt %). The electrolyte/sulfur ratio (E/S) was controlled around 15 and  $6 \mu\text{L mg}^{-1}$  for regular and high-loading electrodes, respectively. The cyclic voltammetry (CV) was measured on the electrochemical workstation (CHI660C, Shanghai CH Instrument Co., Ltd.) at a scanning rate of  $0.1 \text{ mV s}^{-1}$  within the voltage range of 1.7–2.8 V (vs. Li/Li<sup>+</sup>, hereafter inclusive). The electrochemical impedance spectroscopy (EIS) measurement was also performed on CHI660C workstation from the frequency of 0.01 Hz to 100 kHz at an amplitude of 5 mV. The galvanostatic cycling evaluations for cells with different separators were performed on the LAND CT2001A tester.

### 2.5. Computational method

All the calculations were implemented in the Cambridge Serial Total Energy Package based on density functional theory (DFT). Within the generalized gradient approximation (GGA), the revised Perdew-Burke-Ernzerhof exchange-correlation density functional (PBEsol) was applied to describe the exchange-correlation interaction between electrons. The convergence criteria for total energy and ionic force were  $10^{-5} \text{ eV}$  and  $0.03 \text{ eV \AA}^{-1}$ , respectively, to optimize the structure. The cut-off energy of the projector augmented plane-wave basis set was 400 eV, and Monkhorst-Pack grids of  $3 \times 3 \times 2$  and  $2 \times 2 \times 1$  K-points were chosen to describe the Brillouin zone in calculating bulk and surface respectively. After cleaving a surface of facet, a 15 Å vacuum void was built to interrupt atom layers to avoid van der Waals interactions between atoms in neighbour cells.

## 3. Results and discussion

The  $\text{g-C}_3\text{N}_4$  was prepared through a facile one-pot synthesis combining the thermal condensation and oxidization etching processes (see details in Experimental). The reinforced separator was

obtained by simply filtrating the composite of the as-prepared g-C<sub>3</sub>N<sub>4</sub> and CNT onto the conventional polypropylene (PP)-based membrane as illustrated in Fig. 1. The homogenous coating layer can be obtained with a considerable flexibility and mechanical integrity. Such reinforcement layer is expected to benefit the sulfur redox reactions through a typical capture-diffusion-conversion model, where LiPS can be immobilized through the strong physical/chemical interactions with g-C<sub>3</sub>N<sub>4</sub>/CNT, and rapidly converted under the favorable electron/ion support from the porous and conductive framework. As implemented in Li-S batteries, this g-C<sub>3</sub>N<sub>4</sub>/CNT reinforcement layer is likely to build up a robust barrier against the polysulfide shuttling, confining and reutilizing the active sulfur within the cathode for significant improvements in sulfur utilization and reaction reversibility.

To understand the physicochemical characters of the reinforcement agent, the X-ray Diffraction (XRD) pattern of the as-prepared g-C<sub>3</sub>N<sub>4</sub> was firstly collected, which shows a typical main peak at 27.6° and a small peak at 13.3° referring to the (002) and (100) planes, respectively (JCPDS 87-1526, Fig. S1) with a good phase purity [28]. Moreover, the porous texture of g-C<sub>3</sub>N<sub>4</sub> was investigated by N<sub>2</sub> adsorption/desorption measurement as presented in Fig. S2(a). The typical type IV isotherm curve demonstrates the hierarchical porosity with the coexistence of micro-, meso- and macro-porous structures in the obtained g-C<sub>3</sub>N<sub>4</sub>. This favorable feature can be also supported by the pore size distribution in Fig. S2(b), where g-C<sub>3</sub>N<sub>4</sub> shows a wide distribution with a relative concentration at around 1.75 nm. Such characters endow the as-prepared g-C<sub>3</sub>N<sub>4</sub> with a specific surface area of 128.98 m<sup>2</sup> g<sup>-1</sup> and a pore volume of 0.672 cm<sup>3</sup> g<sup>-1</sup> with an average pore size of 1.58 nm based on the BET calculation. The highly porous nature and large specific surface area are expected to not only expose abundant active interfaces for LiPS adsorption, but also facilitate the electrolyte filtration for fast ion transfer, thus leading to strong sulfur immobilization and mitigated electrochemical polarization for sulfur reactions [29].

The morphological structures of g-C<sub>3</sub>N<sub>4</sub> and g-C<sub>3</sub>N<sub>4</sub>/CNT were studied by SEM and TEM characterizations. It can be observed that the prepared g-C<sub>3</sub>N<sub>4</sub> delivers a continuous and porous matrix with wrinkled and thin shells, presenting a sponge-like microstructure (Fig. 2a). The TEM observation further reveals the clear meso-/macropores capsuled by the continuous thin g-C<sub>3</sub>N<sub>4</sub> walls (Fig. 2b), although partially open pore sites can be also observed. These pores are likely formed upon the prolonged thermal condensation and oxidation-etching processes, where the decomposition and condensation of urea form the interconnected continuous skeleton, while the generation of amine gases and the oxidative etching contribute to enriched porosity in the obtained matrix [30]. The selected area electron diffraction (SAED) pattern echoes well with the XRD result, showing two concentric rings assigned to the (100) and (002) planes. Fig. 2(c) shows the dark-field TEM image and Energy Disperse Spectroscopy (EDS) mapping of g-C<sub>3</sub>N<sub>4</sub>, which not only further confirms the thin-shelled porous architecture, but also indicates the homogeneous distribution of C and N in the product. The g-C<sub>3</sub>N<sub>4</sub>/CNT reinforced separator (g-C<sub>3</sub>N<sub>4</sub>/CNT@PP) was prepared through the simple filtration process as described above. Fig. 2(d) presents the SEM image of the g-C<sub>3</sub>N<sub>4</sub>/CNT composite. It can be observed that abundant CNT tightly wrap the g-C<sub>3</sub>N<sub>4</sub> and interconnect with each other to form a long-range continuous framework. Such architecture could effectively enhance the overall conductivity of the composite and thus contribute to a facile implementation of sulfur electrochemical reactions. The thickness of the g-C<sub>3</sub>N<sub>4</sub>/CNT layer was determined around 12 μm (~0.45 mg cm<sup>-2</sup>) by the cross-section SEM observation (Fig. 2e). Meanwhile, the top-view and cross-view element mappings as well as the optical images confirm the uniform coating of the g-C<sub>3</sub>N<sub>4</sub>/CNT composite on one side of the PP membrane (Figs. 2f, S3 and S4).

In addition, X-ray Photoelectron Spectroscopy (XPS) analysis was applied to investigate the surface chemistry of the g-C<sub>3</sub>N<sub>4</sub>. The XPS survey spectrum confirms chemical components of

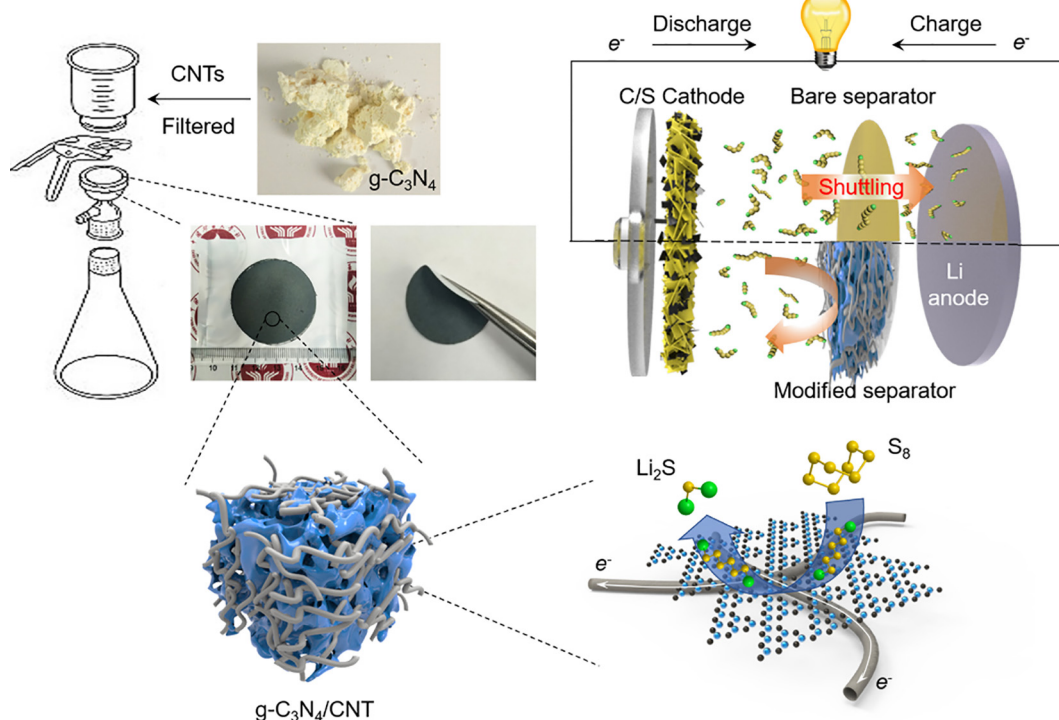


**Fig. 1.** Scheme of the synthesis and function of g-C<sub>3</sub>N<sub>4</sub>/CNT@PP separator.

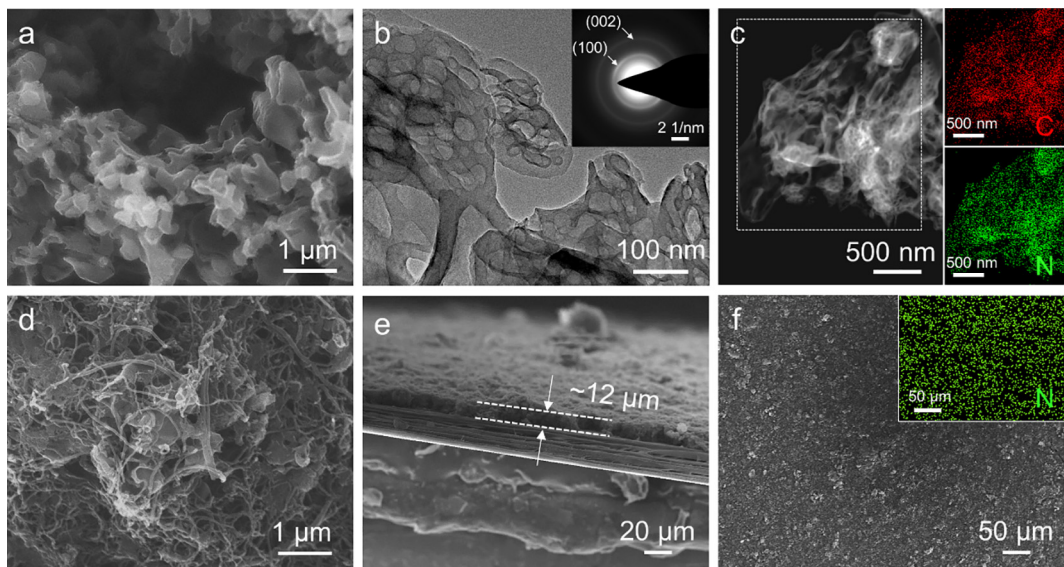


**Fig. 2.** (a) SEM image, (b) TEM image and SAED pattern (inset), (c) dark-field TEM image and element mapping of  $\text{g-C}_3\text{N}_4$ ; (d) SEM image of  $\text{g-C}_3\text{N}_4/\text{CNT}$  composite; (e) cross-view and (f) top-view SEM images with N mapping (inset) of  $\text{g-C}_3\text{N}_4/\text{CNT}@\text{PP}$  separator.

$\text{g-C}_3\text{N}_4$  with the ultrahigh N content as shown in Fig. 3(a). The slight O contamination could be attributed to the partial surface oxidization [31]. The C 1s core-level spectrum can be differentiated into four subpeaks at 284.8, 286.2, 288.2 and 289.3 eV (Fig. 3b), referring to the C–C, C–O, C–N and C=O bonding, respectively [32]. The chemical state of N is analyzed by N 1s spectrum, where the four subpeaks can be assigned to pyridinic N (398.6 eV), pyrrolic N (399.6 eV), graphitic N (400.9 eV) and N-oxide (404.6 eV), respectively (Fig. 3c). The abundant N–C heteroatom structures could induce the electron redistribution on the planar lattice, rendering a polar surface with superior affinity to the weak-polar LiPS species [33,34]. Moreover, pyridinic N has been revealed most LiPS-affiliative among various N states, thus the high content of pyridinic N in the obtained  $\text{g-C}_3\text{N}_4$  could further strengthen the chemical interactions for efficient sulfur immobilization [35].

Given this, the interactions between LiPS and  $\text{g-C}_3\text{N}_4$  was firstly illustrated by the optical LiPS adsorption as displayed in Fig. 3(d) inset. The blank  $\text{Li}_2\text{S}_6$  solution exhibit a light-yellow color, which is basically decolorized after adsorption by  $\text{g-C}_3\text{N}_4$ . Such contrasting variation was further supported by the Ultraviolet–visible (UV-vis) spectra, where the blank  $\text{Li}_2\text{S}_6$  solution shows two typical absorbance peaks at around 350 and 285 nm assigned to  $\text{S}_4^{2-}/\text{S}_6^{2-}$  and  $\text{S}_6^{2-}/\text{S}_8^{2-}$  species, respectively [36]. However, the supernatant after adsorption by  $\text{g-C}_3\text{N}_4$  witnesses drastic declines of these signals, indicating the great diminution of LiPS concentration. These results intuitively validate the great LiPS adsorbability of the obtained  $\text{g-C}_3\text{N}_4$ . The underlying interactive chemistry between LiPS and  $\text{g-C}_3\text{N}_4$  was explored by XPS analysis. As shown in Fig. 3(e), the S 2p spectrum of pure  $\text{Li}_2\text{S}_6$  exhibits typically two peak pairs at 161.0 and 162.5 eV, referring to the sulfur in terminal ( $\text{S}_\text{T}^{-1}$ ) and bridging ( $\text{S}_\text{B}^0$ ) state, respectively [37]. After composited with  $\text{g-C}_3\text{N}_4$ , these characteristic peaks undergo a conspicuous shift to higher binding energy (BE) range, signifying the decrease of electron cloud density in S atoms attributed to the Lewis acid-base interaction between  $\text{Li}_2\text{S}_6$  and  $\text{g-C}_3\text{N}_4$ . Apart from that, the Li 1s spectra witness a clear downshift for the Li–S bond after composited with  $\text{g-C}_3\text{N}_4$ , suggesting the electron transfer from N donor to the Li receptor contributing to “lithium bond”-like N–Li–S bridging configuration [38]. Beyond that, Density Functional Theory (DFT) calculations were carried out to further unveil the interactive chemistry. Fig. 4 shows the geometrically stable

configurations of varied LiPS species adsorbed at pyridinic and pyrrolic N sites on  $\text{g-C}_3\text{N}_4$  surface. It can be observed that Li approaches to the N site for the establishment of the “lithium bond”-like bridging, while the adjacent S prefers the relatively electropositive C site due to the dipolar-dipolar interaction. Such mode echoes well with the XPS results, which describe the interaction behaviors between  $\text{g-C}_3\text{N}_4$  and LiPS. It can be noted that the pyridinic N renders relatively higher LiPS adsorption energies ( $E_{\text{ads}}$ ) than those of pyrrolic N, which is consistent with previous reports [39]. Nevertheless, both these heteroatom structures enable considerably higher  $E_{\text{ads}}$  over pure carbons reported in literatures, demonstrating their great capability of confining LiPS for shuttle inhibition [40].

Based on these results, the functionality of the as-constructed separator was inspected by the LiPS diffusion test in a H-type cell as demonstrated in Fig. S5. The cell was filled with LiPS solution (10 mM  $\text{Li}_2\text{S}_6$ /(DME + DOL)) in one chamber and blank solvent at the other, separated by pristine PP or  $\text{g-C}_3\text{N}_4/\text{CNT}@\text{PP}$  membrane. Apparently, the cell with PP separator undergoes a serious LiPS permeation, which turns the opposite chamber into obvious yellow within 12 h. However, the cell equipped with the reinforced  $\text{g-C}_3\text{N}_4/\text{CNT}@\text{PP}$  separator shows significantly higher resistance to the LiPS permeation, contributing to the minimum color variation upon the diffusion test. This result clearly demonstrates the great capability of the  $\text{g-C}_3\text{N}_4/\text{CNT}@\text{PP}$  separator in obstructing the LiPS migration into the anode, which is highly promising to inhibit the shuttling behaviors in the according Li–S configurations.

To evaluate the practical effect of  $\text{g-C}_3\text{N}_4/\text{CNT}@\text{PP}$  separator in Li–S batteries, S/CNT composite was firstly prepared through the conventional melt-diffusion method. The S content was determined ca. 72 wt% by the Thermogravimetry analysis (TGA, Fig. S6). CR2032 coin cells were fabricated based on the S/CNT cathode and different separators for the electrochemical characterizations. Fig. 5(a) depicts the CV curves of the cells with pristine PP,  $\text{g-C}_3\text{N}_4@\text{PP}$  and  $\text{g-C}_3\text{N}_4/\text{CNT}@\text{PP}$  separators. All of them show typically two reduction peaks upon the cathodic scanning, corresponding to the electrochemical reduction of elemental sulfur into high-ordered soluble polysulfides ( $\text{Li}_2\text{S}_x$ ,  $4 < x \leq 8$ ) and their further transformation into insoluble  $\text{Li}_2\text{S}_2$  and  $\text{Li}_2\text{S}$ . Meanwhile, the overlapped peaks upon the anodic scanning can be ascribed to the reversed sulfur oxidation process [41,42]. By comparison, the  $\text{g-C}_3\text{N}_4/\text{CNT}@\text{PP}$  cell

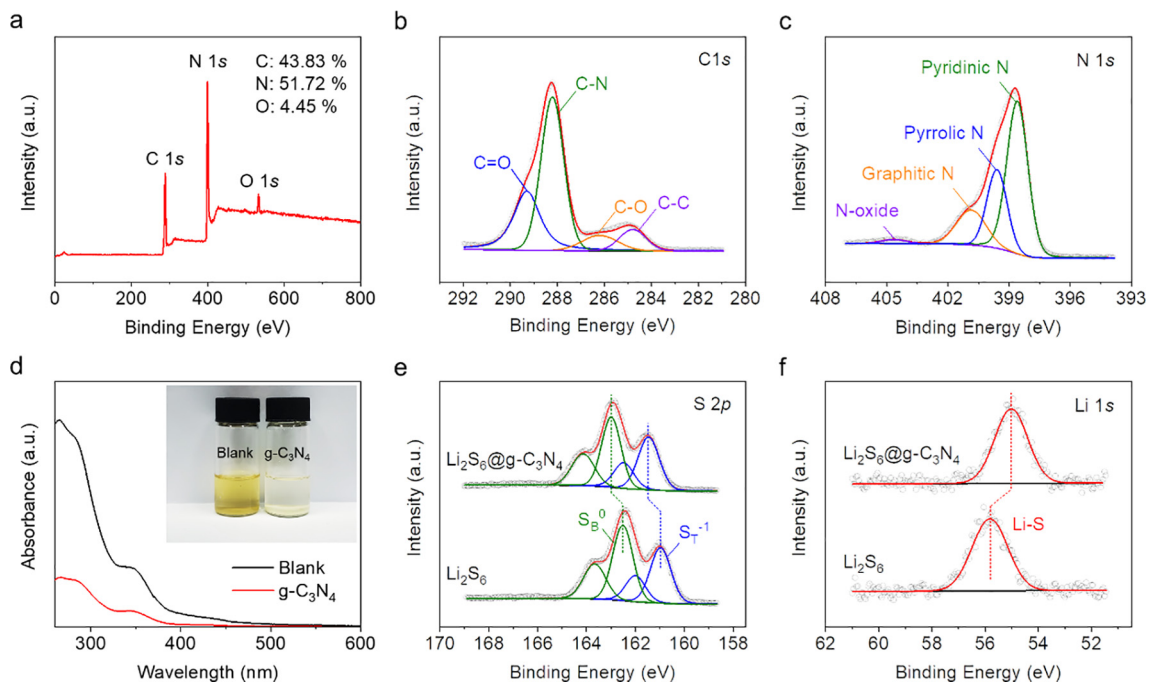


**Fig. 3.** XPS (a) survey, (b) C 1s, and (c) N 1s spectra of g-C<sub>3</sub>N<sub>4</sub>; (d) UV-vis spectra with the optical comparison (inset) of LiPS solution before and after adsorption; (e) XPS S 2p and (f) Li 1s spectra of Li<sub>2</sub>S<sub>6</sub> before and after adsorption.

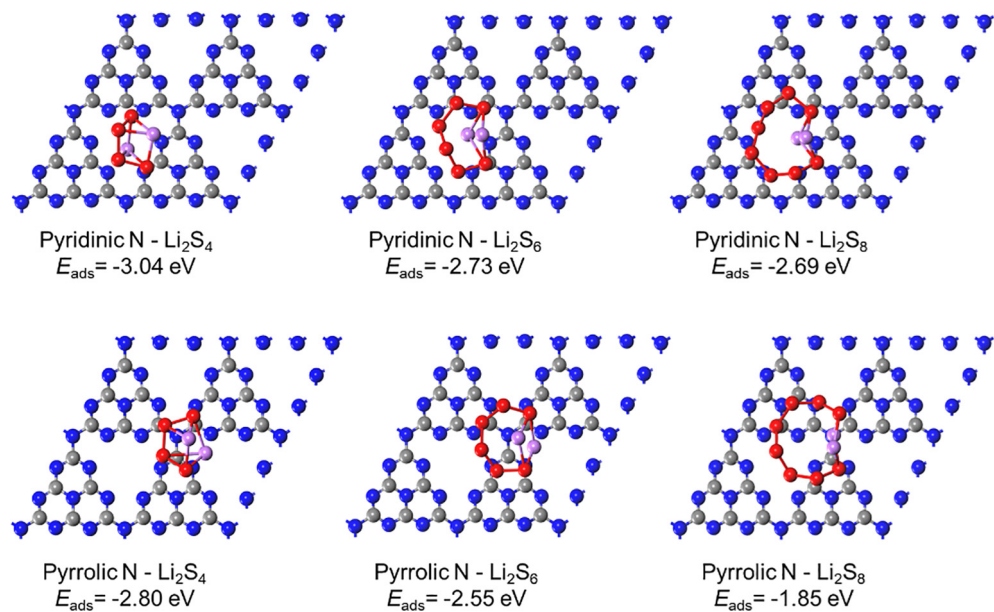


**Fig. 4.** Geometrically stable configurations of varied LiPS (Li<sub>2</sub>S<sub>4</sub>, Li<sub>2</sub>S<sub>6</sub>, and Li<sub>2</sub>S<sub>8</sub>) adsorbed at pyridinic and pyrrolic N sites on g-C<sub>3</sub>N<sub>4</sub> surface with the corresponding adsorption energies. The black, blue, red, and pink balls refer to C, N, S and Li atom respectively.

exhibits the highest current response and the lowest potential hysteresis for the redox peaks, indicating its lowest electrochemical polarization and fastest reaction kinetics. The voltage profiles present good consistency with the CV results, showing a two-platform discharge curve and a long charging slope (Fig. 5b). The voltage hysteresis between charge and discharge is ca. 0.20, 0.17 and 0.16 V for the cell with PP, g-C<sub>3</sub>N<sub>4</sub>@PP, and g-C<sub>3</sub>N<sub>4</sub>/CNT@PP separator, respectively, confirming the smallest overpotentials in g-C<sub>3</sub>N<sub>4</sub>/CNT@PP-based configuration. This result receives further support from the EIS analysis in Figs. 5(c) and S7. The Nyquist plots of the cells comprise a compressed semicircle at high-medium

frequency and a slope at low frequency, which reflects the charge-transfer resistance ( $R_{ct}$ ) and Warburg resistance, respectively [43]. Clearly, both the EIS results before and after cycling demonstrate the smallest internal impedance for the g-C<sub>3</sub>N<sub>4</sub>/CNT@PP cell, further confirming its facilitated sulfur reactions compared with other samples. Such kinetic improvement is spurred by the strong LiPS adsorbability of g-C<sub>3</sub>N<sub>4</sub>, which enhances the LiPS concentration on electrode surface and thus promotes the conversion reactions in g-C<sub>3</sub>N<sub>4</sub>@PP cell than that with pristine PP separator. Apart from that, the integration of CNT constructs extensive and long-range electron highways, which further facilitates the sulfur

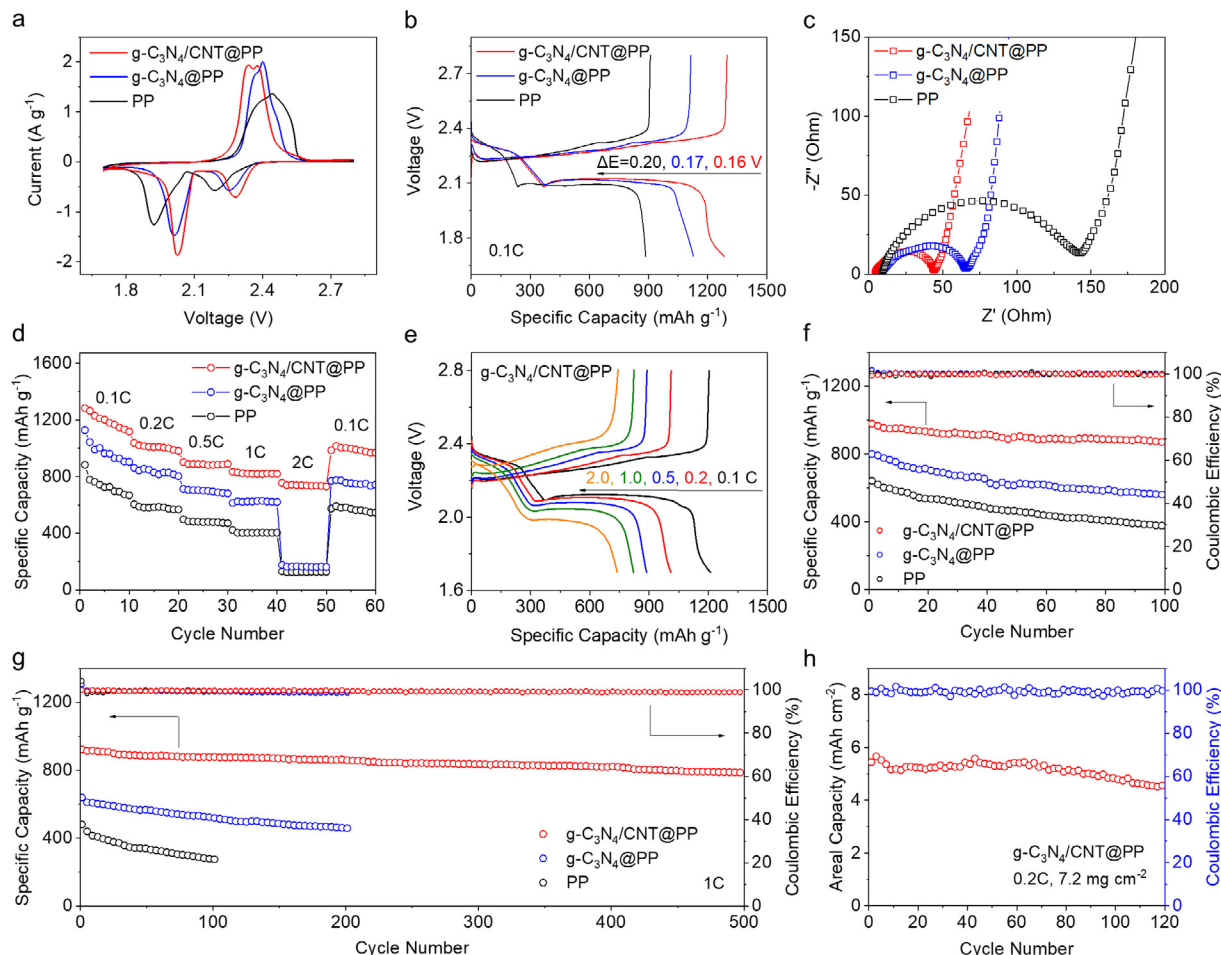


**Fig. 5.** (a) CV profiles, (b) voltage profiles, (c) Nyquist plots, and (d) rate performances of cells with PP, g-C<sub>3</sub>N<sub>4</sub>@PP, and g-C<sub>3</sub>N<sub>4</sub>/CNT@PP separators; (e) voltage profiles of g-C<sub>3</sub>N<sub>4</sub>/CNT@PP cell at varied rates; cycling comparison between different cells at (f) 0.2 C and (g) 1 C; (h) cycling performance of g-C<sub>3</sub>N<sub>4</sub>/CNT@PP cell at a raised sulfur loading of 7.2 mg cm<sup>-2</sup>.

electrochemical reactions, thus leading to the best kinetic behaviors of the g-C<sub>3</sub>N<sub>4</sub>/CNT@PP cell. Benefiting from these features, the cell equipped with the g-C<sub>3</sub>N<sub>4</sub>/CNT@PP separator achieves the best rate capability, exhibiting a high capacity of 755.5 mAh g<sup>-1</sup> at a decent current rate of 2 C. By contrast, the PP and g-C<sub>3</sub>N<sub>4</sub>@PP cells undergo much faster capacity decay upon the raise of current rate (Fig. 5d). The improvement in rate performance can be further understood from the voltage profile variations. As shown in Fig. 5(e), the g-C<sub>3</sub>N<sub>4</sub>/CNT@PP cell maintains the clear two-plateau discharge profile even under a considerable rate up to 2 C, indicating its limited electrochemical overpotentials and fast reaction kinetic. In comparison, the voltage profiles of PP and g-C<sub>3</sub>N<sub>4</sub>@PP cells experience serious polarization with much larger charge-discharge potential gap and even fail to present the second discharge plateau at high rate within the testing voltage range (Fig. S8). All these results evidently confirm the significant improvement of sulfur reaction kinetics by the implementation of g-C<sub>3</sub>N<sub>4</sub>/CNT@PP separator.

The galvanostatic cycling comparison at 0.2 C was depicted in Fig. 5(f). The g-C<sub>3</sub>N<sub>4</sub>/CNT@PP separator enables the best cycling stability with a high capacity retention of 870.5 mAh g<sup>-1</sup> after 100 cycles. This should be attributed to the strong LiPS adsorption by g-C<sub>3</sub>N<sub>4</sub>, which effectively immobilizes the active species and reduces their consumption by shuttle effect. In addition, the incorporation CNT facilitates the reutilization of the adsorbed LiPS and further strengthens the shuttle inhibition, thus fulfilling the significant enhancement in capacity and cyclability. The impact of conductive agent in the reinforcement layer was studied by replacing

CNT with conventional super P (SP) as shown in Fig. S9. It can be perceived that the cell based on g-C<sub>3</sub>N<sub>4</sub>/SP@PP separator exhibits improved reaction kinetics and cyclability than those with PP and g-C<sub>3</sub>N<sub>4</sub>@PP separators, but still relatively inferior to that equipped with g-C<sub>3</sub>N<sub>4</sub>/CNT@PP. This is mainly due to the intrinsically higher conductivity and larger surface area of CNT over SP. Besides, the 1D long-range-extended CNT could intertwine with each other and tightly overlay the g-C<sub>3</sub>N<sub>4</sub>, contributing to the significant improvement in overall electron/ion transfer within the electrode. Given this, long-term cycling comparison was further conducted as shown in Fig. 5(g). The g-C<sub>3</sub>N<sub>4</sub>/CNT@PP cell delivers an excellent cycling stability with a minimum capacity fading rate of 0.03% per cycle during the 500 cycles at 1 C, whereas the g-C<sub>3</sub>N<sub>4</sub>@PP and PP cells undergo much faster capacity decay ascribed to the lack of sulfur confinement. Moreover, a high coulombic efficiency can be maintained consistently over the long-term cycling, indicating the good electrochemical reversibility in g-C<sub>3</sub>N<sub>4</sub>/CNT@PP-based configuration. This great improvement in cycling stability further illustrates the great capability of the reinforced separator in suppressing the shuttle effect and stabilizing the Li-S battery chemistry. Furthermore, cycling evaluation on g-C<sub>3</sub>N<sub>4</sub>/CNT@PP cells with higher sulfur loading was attempted in pursuit of higher energy density. Benefiting from the favorable LiPS regulation, the g-C<sub>3</sub>N<sub>4</sub>/CNT@PP separator enables a high areal capacity of 5.67 mAh cm<sup>-2</sup> with an increased sulfur loading of 7.2 mg cm<sup>-2</sup> (Fig. 5h), which is competitive to the commercialized Li-ion counterpart (~4 mAh cm<sup>-2</sup>) [44]. Moreover, a decent cycla-

bility can be also obtained retaining 4.56 mAh cm<sup>-2</sup> after 120 cycles. In addition, more aggressive attempt was carried out with an even higher sulfur loading of 10.1 mg cm<sup>-2</sup>, which renders an attractively high areal capacity of 7.69 mAh cm<sup>-2</sup>, yet suffers from a relatively poor capacity retention particularly during the first several cycles (Fig. S10). It should be noted that the achieved battery performances under both regular and high-loading configurations are highly competitive among the cells with modified separators in recent literatures (Tables S1 and S2), although further advances are still required potentially consisting in separator optimization as well as its cooperation with rational cathode constructions. Overall, these results strongly demonstrate the good promise of the as-designed separator reinforcement in the development of superior Li-S batteries for practical applications.

#### 4. Conclusions

In summary, a g-C<sub>3</sub>N<sub>4</sub>/CNT composite reinforced separator was developed to improve the Li-S battery performance. The polar nature, high N content and sponge-like microstructure of the obtained g-C<sub>3</sub>N<sub>4</sub> impose potent sulfur immobilization benefiting from its strong chemical interactions with LiPS. Meanwhile, the integration of CNT establishes an interconnected long-range conductive framework for fast electron/ion transfers. Attributed to these synergistic benefits, the g-C<sub>3</sub>N<sub>4</sub>/CNT modified separator renders a favorable polysulfide barrier that effectively obstructs the LiPS penetration and enhances their reutilization, thus contributing to suppressed shuttle effect, promoted reaction kinetics, and stabilized sulfur electrochemistry. The cells based on the g-C<sub>3</sub>N<sub>4</sub>/CNT@PP separator exhibit excellent cycling stability and rate capability, as well as decent capacity and cyclability under high-loading configuration. This work provides a facile approach to the highly effective polysulfide barrier, holding a good promise to promote the future development of high-performance Li-S batteries.

#### Declaration of Competing Interest

The authors declare that they have no known competing financial interests or personal relationships that could have appeared to influence the work reported in this paper.

#### Acknowledgments

This work is supported by the National Natural Science Foundation of China (Nos. 21978110 and 51772126), Natural Science Foundation of Beijing (No. L182062), Organization Department of Beijing Talents Project (2018000021223ZK21), the Yue Qi Young Scholar Project of China University of Mining & Technology (Beijing) (No. 2017QN17), the Fundamental Research Funds for the Central Universities (No. 2014QJ02), Jilin Province Science and Technology Department Program (Nos. 20200201187JC, 20190201309JC, and 20190101009JH), the “13th five-year” Science and Technology Project of Jilin Provincial Education Department (No. JJKH20200407KJ), Jilin Province Development and Reform Commission Program (Nos. 2020C026-3 and 2019C042-1) and Jilin Province Fund for Talent Development Program (No. [2019] 874). The authors also thank the supports from Natural Sciences and Engineering Research Council of Canada (NSERC), the University of Waterloo, and the Waterloo Institute for Nanotechnology.

#### Appendix A. Supplementary data

Supplementary data to this article can be found online at <https://doi.org/10.1016/j.jec.2020.05.036>.

#### References

- [1] M.K. Song, E.J. Cairns, Y.G. Zhang, *Nanoscale* 5 (2013) 2186–2204.
- [2] Z.Y. Xing, G.R. Li, S. Sy, Z.W. Chen, *Nano Energy* 54 (2018) 1–9.
- [3] P. Liu, Y. Wang, J. Liu, *J. Energy Chem.* 34 (2019) 171–185.
- [4] G.R. Li, Z.W. Chen, J. Lu, *Chem* 4 (2018) 3–7.
- [5] T. Ould Ely, D. Kamzabek, D. Chakraborty, M.F. Doherty, *ACS Appl. Energy Mater.* 1 (2018) 1783–1814.
- [6] J.L. Yang, S.X. Zhao, Y.M. Lu, X.T. Zeng, W. Lv, G.Z. Cao, *Nano Energy* 68 (2020) 104356.
- [7] Q. Qi, X. Lv, W. Lv, Q.H. Yang, *J. Energy Chem.* 39 (2019) 88–100.
- [8] G.R. Li, W. Lei, D. Luo, Y.P. Deng, Z.P. Deng, D.L. Wang, A.P. Yu, Z.W. Chen, *Energy Environ. Sci.* 11 (2018) 2372–2381.
- [9] R.P. Liu, F. Guo, X.F. Zhang, J. Yang, M. Li, W. Miaomiao, H. Liu, M. Feng, L. Zhang, *ACS Appl. Energy Mater.* 2 (2019) 1348–1356.
- [10] M. Zhao, B.Q. Li, H.J. Peng, H. Yuan, J.Y. Wei, J.Q. Huang, *Angew. Chem. Int. Ed.* (2019), <https://doi.org/10.1002/anie.201909339>.
- [11] R. Wu, S. Chen, J. Deng, X. Huang, Y. Song, R. Gan, X. Wan, Z. Wei, *J. Energy Chem.* 27 (2018) 1661–1667.
- [12] M.R. Wang, X.F. Zhou, X. Cai, H.Q. Wang, Y.P. Fang, X.H. Zhong, *J. Energy Chem.* 50 (2020) 106–114.
- [13] X. Li, Z. Pan, Z. Li, X. Wang, B. Saravanakumar, Y. Zhong, L. Xing, M. Xu, C. Guo, W. Li, *J. Power Sources* 420 (2019) 22–28.
- [14] Z.M. Cui, C.X. Zu, W.D. Zhou, A. Manthiram, J.B. Goodenough, *Adv. Mater.* 28 (2016) 6926.
- [15] J.N. Wang, Y.P. Li, W.W. Li, C.Z. Sun, C.Y. Qi, J. Jin, Z.Y. Wen, *Chemistryselect* 4 (2019) 7102–7107.
- [16] W.Z. Bao, L. Liu, C.Y. Wang, S. Choi, D. Wang, G.X. Wang, *Adv. Energy Mater.* 8 (2018) 1702485.
- [17] G. Cui, G. Li, D. Luo, Y. Zhang, Y. Zhao, D. Wang, J. Wang, Z. Zhang, X. Wang, Z. Chen, *Nano Energy* 72 (2020) 104685.
- [18] S.H. Chung, A. Manthiram, *J. Phys. Chem. Lett.* 5 (2014) 1978–1983.
- [19] G.M. Zhou, S.F. Pei, L. Li, D.W. Wang, S.G. Wang, K. Huang, L.C. Yin, F. Li, H.M. Cheng, *Adv. Mater.* 26 (2014) 625–631.
- [20] S.H. Chung, A. Manthiram, *Adv. Mater.* 26 (2014) 7352–7357.
- [21] M. Inagaki, T. Tsumura, T. Kinumoto, M. Toyoda, *Carbon* 141 (2019) 580–607.
- [22] D.R. Deng, C.D. Bai, F. Xue, J. Lei, P. Xu, M.S. Zheng, Q.F. Dong, *ACS Appl. Mater. Interfaces* 11 (2019) 11474–11480.
- [23] Z. Jia, H. Zhang, Y. Yu, Y. Chen, J. Yan, X. Li, H. Zhang, *J. Energy Chem.* 43 (2020) 71–77.
- [24] J. Liu, W. Li, L. Duan, X. Li, L. Ji, Z. Geng, K. Huang, L. Lu, L. Zhou, Z. Liu, W. Chen, L. Liu, S. Feng, Y. Zhang, *Nano Lett.* 15 (2015) 5137–5142.
- [25] L. Qu, P. Liu, Y. Yi, T. Wang, P. Yang, X. Tian, M. Li, B. Yang, S. Dai, *ChemSusChem* 12 (2019) 213–223.
- [26] J. Wang, Z. Meng, W. Yang, X. Yan, R. Guo, W.Q. Han, *ACS Appl. Mater. Interfaces* 11 (2019) 819–827.
- [27] Y.G. Huangfu, T.T. Zheng, Kun Zhang, X.J. She, H. Xu, Z. Fang, K.Y. Xie, *Electrochim. Acta* 272 (2018) 60–67.
- [28] D. Zhou, C. Qiu, *Chem. Phys. Lett.* 728 (2019) 70–73.
- [29] Y.Z. Song, S.Y. Zhao, Y.R. Chen, J.S. Cai, J. Li, Q.H. Yang, J.Y. Sun, Z.F. Liu, *ACS Appl. Mater. Interfaces* 11 (2019) 5687–5694.
- [30] D.R. Paul, S. Gautam, P. Panchal, S.P. Nehra, P. Choudhary, A. Sharma, *ACS Omega* 5 (2020) 3828–3838.
- [31] Y.F. Li, R.X. Jin, Y. Xing, J.Q. Li, S.Y. Song, X.C. Liu, M. Li, R.C. Jin, *Adv. Energy Mater.* 6 (2016) 1601273.
- [32] Z.H. Sheng, L. Shao, J.J. Chen, W.J. Bao, F.B. Wang, X.H. Xia, *ACS Nano* 5 (2011) 4350–4358.
- [33] X. Chen, X.R. Chen, T.Z. Hou, B.Q. Li, X.B. Cheng, R. Zhang, Q. Zhang, *Sci. Adv.* 5 (2019), eaau7728.
- [34] X. Li, X. Li, M.N. Banis, B. Wang, A. Lushington, X. Cui, R. Li, T.-K. Sham, X. Sun, *J. Mater. Chem. A* 2 (2014) 12866.
- [35] L.C. Yin, J. Liang, G.M. Zhou, F. Li, R. Saito, H.M. Cheng, *Nano Energy* 25 (2016) 203–210.
- [36] S.P. Li, Z.L. Han, W. Hu, L.F. Peng, J.Q. Yang, L.H. Wang, Y.Y. Zhang, B. Shan, J. Xie, *Nano Energy* 60 (2019) 153–161.
- [37] Y.K. Wang, R.F. Zhang, J. Chen, H. Wu, S.Y. Lu, K. Wang, H.L. Li, C.J. Harris, K. Xi, R.V. Kumar, S.J. Ding, *Adv. Energy Mater.* 9 (2019), 1900953.
- [38] X. Wang, C. Yang, X. Xiong, G. Chen, M. Huang, J.H. Wang, Y. Liu, M. Liu, K. Huang, *Energy Storage Mater.* 16 (2019) 344–353.
- [39] F.G. Sun, J.T. Wang, H.C. Chen, W.C. Li, W.M. Qiao, D.H. Long, L.C. Ling, *ACS Appl. Mater. Interfaces* 5 (2013) 5630–5638.
- [40] F. Pei, L. Lin, A. Fu, S. Mo, D. Ou, X. Fang, N. Zheng, *Joule* 2 (2018) 323–336.
- [41] J. Pu, Z.H. Shen, J.X. Zheng, W.L. Wu, C. Zhu, Q.W. Zhou, H.G. Zhang, F. Pan, *Nano Energy* 37 (2017) 7–14.
- [42] J. Zhang, W.Z. Ma, Z.Y. Feng, F.F. Wu, D.H. Wei, B.J. Xi, S.L. Xiong, *J. Energy Chem.* 39 (2019) 54–60.
- [43] X. Tang, Z. Sun, H. Yang, H. Fang, F. Wei, H.-M. Cheng, S. Zhuo, F. Li, *J. Energy Chem.* 31 (2019) 119–124.
- [44] H.J. Peng, W.T. Xu, L. Zhu, D.W. Wang, J.Q. Huang, X.B. Cheng, Z. Yuan, F. Wei, Q. Zhang, *Adv. Funct. Mater.* 26 (2016) 6351–6358.